Received: 12 May 2021 | Revised: 12 October 2021 | Accepted: 14 October 2021

DOI: 10.1111/bre.12626

Basin Research IAS EAGE WILEY

RESEARCH ARTICLE

Influence of variable decoupling between vertically separated fault populations on structural inheritance – The Laminaria High, NW Shelf of Australia

Thomas B. Phillips | **Ken McCaffrey** | **Luke Magarinos**

Department of Earth Science, Science Labs, Durham University, Durham, UK

Correspondence
Thomas B. Phillips, Department of Earth Science, Science Labs, Durham University, Durham, UK.
Email: thomas.b.phillips@durham.ac.uk

Funding information
The Leverhulme Trust

Abstract

When extension events are greatly separated in time, older faults may be buried and stratigraphically separated from newly developing faults at shallower depths. During rifting, the buried structures may reactivate and propagate upwards to be expressed within the shallow system. The degree of linkage between structural levels determines the influence that the deeper structures can exert over the geometry and evolution of the incipient fault system. In this study we use 3D seismic reflection data to examine how a deep fault population across the Laminaria High, NW shelf of Australia influences the development of a younger fault system at shallow depths. These fault populations are non-parallel and decoupled across a mechanically weak interval. The majority of shallow faults are not linked to those at depth. However, the reactivation and upward propagation of some of the deeper faults produce anomalously oriented structures at shallow depths, hard-linked to the deeper structures. One fault in particular shows along-strike variability, with the deep segment reactivated and present at shallow depths in the west. To the east, the shallow and deep fault segments become decoupled across the mechanically weak interval, although some soft-linkage and strain transfer still occurs. We suggest that this switch in the degree of coupling along the fault is due to the geometry of the deeper structure, with the transition corresponding to a prominent relay ramp. We show how the geometry of a deeper fault may affect its propensity to reactivate during subsequent extensional events, ultimately affecting the degree of structural inheritance that is expressed within younger, shallower fault populations.

KEYWORDS

rifting, fault reactivation, structural inheritance, seismic reflection

1 | INTRODUCTION

During extension, faults formed during earlier rift phases exert variable degrees of influence over the geometric and kinematic evolution of the incipient fault population (Henstra et al., 2019; Henza et al., 2011; Reeve et al., 2015; Whipp et al., 2014). Younger faults may completely or partially reactivate older structures (e.g. Duffy et al., 2015; Nixon et al., 2014; Whipp et al., 2014), or they may be segmented by or completely ignore the pre-existing fault population (e.g. Claringbould et al., 2017; Deng et al., 2017; Henstra et al., 2019). The potential for this structural inheritance of the geometric properties of pre-existing faults by younger ones is governed by multiple factors, including the orientation of the principal stress axes during each rift event (Henza et al., 2011), the magnitude of the prior rift phase (Henstra et al., 2019; Henza et al., 2010) and the mechanical properties of the stratigraphic units (Lewis et al., 2013).

When extensional events are greatly separated in time, newly formed fault populations may be stratigraphically and vertically separated from older, often buried, fault populations, meaning that plan–view relationships may not be informative (Çiftçi & Langhi, 2012; Collanega et al., 2019). Furthermore, the presence of ductile units such as salt or shale may vertically partition strain and further decouple fault populations, thus producing a strong influence over the basin geometry and stratigraphy as well as fluid flow and fracture distribution across and surrounding the ductile, incompetent interval, (Bell, 1996; Coleman et al., 2017; Gartrell et al., 2003, 2004; Lewis et al., 2013; O'Sullivan et al., 2021; Shipilin et al., 2020). At present, it remains unclear how strain is distributed and partitioned between vertically separated fault networks, and what effect, if any, the deeper fault population may exert over incipient faults in these instances.

In this study, we investigate how a pre-existing fault population at depth influences the development of a stratigraphically shallower fault population, separated by an intervening decoupling interval. More specifically, we examine the causes behind along-strike variations in geometric and kinematic linkage between deep and shallow structural levels, which ultimately influence the degree of structural inheritance expressed in the geometric properties of the shallow fault population. To accomplish this, we analyse a borehole-constrained 3D seismic reflection volume across the Laminaria High along the northern margin of the NW shelf of Australia (Figure 1a). This area is characterised by an E–W oriented fault population at depth, formed during Late Jurassic–Cretaceous extension, overlain by a WSW–ENE oriented fault population at shallow depths formed due to Plio-Pleistocene lithospheric flexure associated with subduction occurring to the north (Figure 1b; Çiftçi & Langhi, 2012; Keep et al., 2002; Langhi et al., 2011; Langhi & Borel, 2008; Saqab et al., 2017). The shallow grabens often overlie deeper horsts, forming hourglass-type structures, with the two fault populations largely separated by a mechanically incompetent, shale-dominated stratigraphic interval (Figure 2a; Çiftçi & Langhi, 2012).

Highlights

- We map two non-collinear fault systems
- vertically separated by a mechanically incompetent unit
- Variable along-strike coupling between fault populations influences fault geometry and structural inheritance at shallow depths
- The transition between hard- and soft-linked fault segments is controlled by a relay ramp along the deeper fault

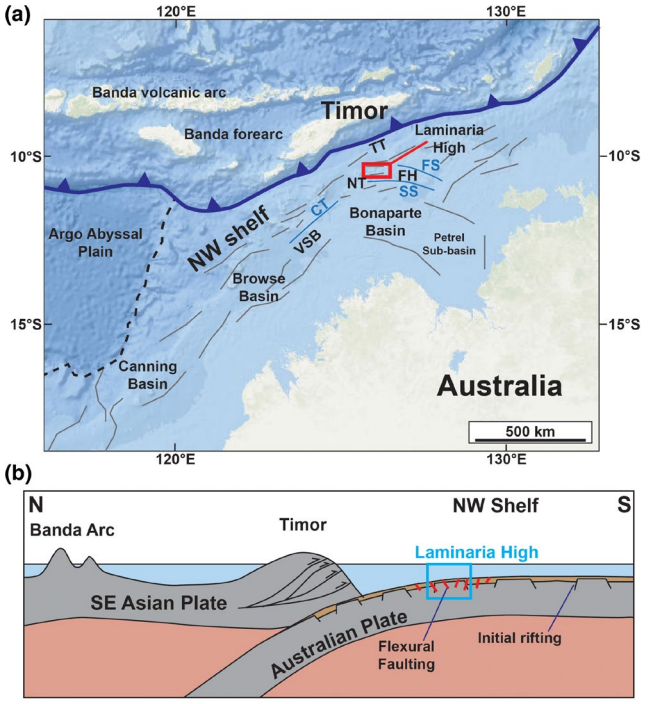

FIGURE 1 (a) Regional map showing the location of the study area along with key geological features along the NW Shelf of Australia. CT, Cartier Trough; FH, Flamingo High; FS, Flamingo Syncline; NT, Nancar Trough; SS, Sahul Syncline; TT, Timor Trough; VSB, Vulcan sub-basin. Structural elements after Langhi et al., 2013. (b) Schematic cross-section highlighting the northern Australian margin being subducted beneath the East Timor subduction zone to the north. Flexural faulting related to this subduction occurs across the Laminaria High. After Çiftçi and Langhi (2012)

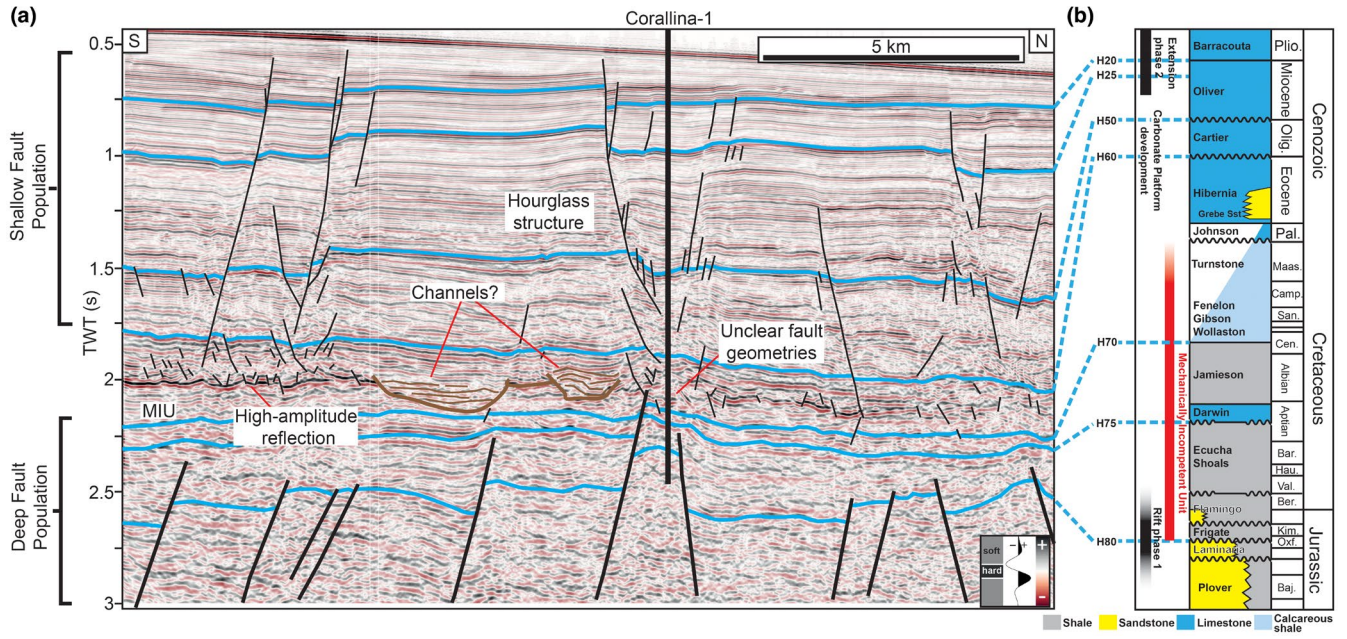

FIGURE 2 (a) Interpreted seismic section across the Laminaria High, highlighting the deep and shallow fault populations and key stratigraphic horizons across the section. The mechanically incompetent unit (MIU) spans from H80 to above H70. (b) Stratigraphic column for the Laminaria High, after Abbassi et al. (2015) and de Ruig et al. (2000). The main rift phases occur in the Late Jurassic and Miocene–Pliocene. Polarity cartoon after https://agile.geosci.ai/polarity. Uninterpreted version of this section can be found as Figure S1

We find that, aside from the co-location of shallow graben above deeper horsts in some areas, the orientation of the shallow fault population is largely independent of the deeper structures, with the shallow faults paralleling the subduction front to the north. However, we note that some older faults extend upwards to shallow depths, producing anomalously oriented structures at shallow depths. We show that the reactivation of deeper faults is modulated by their size, detailed structure and orientation, with larger structures more likely to reactivate. However, prominent relay zones along the faults may partition the reactivation of fault segments, producing areas of hard and soft vertical linkage across the weak interval. We show how the geometry and structure of deeper faults results in a variable degree of reactivation and linkage between structural levels, influencing the orientation and spatial distribution of later-formed structures and exerting a variable degree of structural inheritance over the shallow fault population.

2 | GEOLOGICAL SETTING

2.1 | Structural evolution of the Laminaria High

The Laminaria High is located on the northwest shelf of Australia, along the northern margin of the Bonaparte Basin (Figure 1a; Çiftçi & Langhi, 2012; Langhi & Borel, 2008). The high is located on the boundary between the continental shelf and slope, which plunges northwards into the East Timor subduction zone (Langhi et al., 2011; Saqab et al., 2017). The study area is bound to the south by the Nancar Trough and Vulcan Subbasin, the Flamingo and Sahul synclines to the east, and the Timor Trough to the north and west (Figure 1a; Abbassi et al., 2015; Çiftçi & Langhi, 2012).

The Bonaparte Basin, including the Laminaria High, experienced three phases of extension throughout its evolution. An initial phase of rifting occurred during the Late Devonian-Early Carboniferous, producing the NW–SE oriented structures adjacent to the Laminaria High, including the Nancar Trough and Flamingo syncline (Langhi & Borel, 2008; O'Brien et al., 1993). A second phase of rifting occurred during the Carboniferous-Permian, associated with the initiation and propagation of the Neo-Tethys rift systems; this rift phase was associated with the formation of the NE–SW oriented Westralian Superbasin across the NW shelf of Australia (Yeates et al., 1987), which includes the Bonaparte, Browse and Canning Basins (Figure 1a; Jablonski & Saitta, 2004; Langhi & Borel, 2005). A further rift event related to the breakup of Gondwana and associated with the formation of the Argo Abyssal Plain occurred during the Late Jurassic (de Ruig et al., 2000). This latter rift phase imparted a NE–SW oriented fabric across the majority of the region, and an E–W fabric

across the Laminaria High, likely related to pre-existing structures associated with the earlier events (Çiftçi & Langhi, 2012). Across the Laminaria High this Late Jurassic rift phase was associated with the formation of E–W trending faults, forming the horst and graben rift physiography identified at deep structural levels (Figure 2a). This extension was also associated with a period of Late Jurassic uplift related to the onset of seafloor spreading (Harrowfield & Keep, 2005).

During the Miocene-Pliocene, the northern margin of the Australian Plate collided with the Banda Arc, leading to the onset of subduction and the associated flexure of the downgoing Australian plate to the south (Figure 1b; Langhi et al., 2011; Saqab et al., 2017). Flexure of the Australian plate led to a prevalent NNW–SSE oriented extension across the Laminaria High, and the formation of WSW–ENE oriented flexure-related faults at shallow depths (Langhi et al., 2011). Some faults extend up to the seabed, indicating that they may be active at the present day. The maximum extension, and likely the peak fault activity, occurred during the Pliocene, when the Laminaria High was situated atop the forebulge of the downgoing plate (Saqab et al., 2017).

2.2 | Laminaria High stratigraphy

Syn-rift strata at the base of the imaged seismic section are associated with Late Jurassic extension and comprise the deltaic-to-shallow marine Plover and Laminaria sandstones (Figure 2b; Abbassi et al., 2015; Çiftçi & Langhi, 2012; Labutis & Ruddock, 1998). Following Late Jurassic extension, the Laminaria High was tectonically quiescent throughout the Early Cretaceous, leading to the deposition of a thick shale-dominated interval (Figure 2b; Abbassi et al., 2015; Çiftçi & Langhi, 2012). Subsequently, accommodation space across the margin was filled by prograding wedges, with the carbonate content increasing upwards through the succession and eventually leading to the establishment of the area as a carbonate platform by the Late Cretaceous. This carbonate platform persisted throughout the Cenozoic (Abbassi et al., 2015; Abdulkareem et al., 2019).

The stratigraphy across the Laminaria High can be broadly divided into three main intervals: syn-rift sandstones at depth associated with Late Jurassic extension, an overlying shale-dominated succession associated with a period of tectonic quiescence and the deepening continental shelf, and the establishment of a carbonate platform during the Cenozoic. Çiftçi and Langhi (2012) assign mechanical properties to these broad intervals, suggesting that the shale dominated sequence (H80 to ca. H60) represents a mechanically incompetent unit (MIU), herein referred to as the MIU, bounded above and below by more competent units dominated by carbonate and sandstone, respectively (Figure 2b).

3 | DATA AND METHODS

In this study we examine the Laminaria 3D seismic volume covering a ca. 680 km^2 area of the Laminaria High. The seismic volume records to 3 s TWT depth and has an inline and crossline spacing of 12.5 m. Seismic data are recorded as zero-phase and follow the SEG reverse polarity convention. A downward increase in impedance is represented by a trough (red), whereas a downward decrease in impedance is represented by a peak (black; Figure 2). Images are shown at 5× vertical exaggeration. Seismic imaging is of a good quality across the area, particularly in the shallow section where a high signal-to-noise ratio resolves clearly defined faults (Langhi et al., 2011). Image quality decreases with depth such that interpretations are of lower confidence at deeper levels, although we were able to identify major faults in this interval, in agreement with other studies in the area (Çiftçi & Langhi, 2012; Figure 2a).

We mapped eight borehole-constrained stratigraphic horizons, including the seabed, throughout the volume (Figure 2a). These horizons were constrained by the Vidalia-1, Corallina-1 and Laminaria-1 boreholes, along with information from previous studies in the area (Çiftçi & Langhi, 2012). We focussed on mapping prominent reflections throughout the data and subsequently linked our interpretations to the stratigraphic framework provided by de Ruig et al. (2000) and Abbassi et al. (2015). The mapped horizons were as follows: (a) Top Oxfordian (H80); (b) Aptian (H75); (c) Cenomanian (H70); (d) Base Oligocene (H60); (e) Base Miocene (H50); (f) Late Miocene (H25); (g) Base Pliocene (H20) and (h) the seabed (Figure 2). In addition, we mapped a high-amplitude, laterally discontinuous reflection within the H60-H70 interval where possible, referred to as the high-amplitude reflection. Uninterpreted seismic sections are shown in the Supporting Information (Figures S1–S4).

To examine the evolution of faults and to understand the vertical linkage between the deep and shallow structural levels across the Laminaria High, we undertook quantitative fault analyses. Throw-length (*T-x*) and throw-depth (*T-z*) analysis enables us to elucidate the geometric and kinematic evolution of faults. *T-x* analyses were undertaken along faults across multiple structural levels (Duffy et al., 2015; Walsh et al., 2003). Measurements were taken at intervals of 50 crossline intervals (equivalent to 625 m), oriented perpendicular to the main fault strike. By using crosslines, we are able to account for changes in fault orientation at different

structural levels and collapse measurements of overlapping fault segments onto a single profile. We also carried out the *T-z* analyses at multiple points to understand the vertical linkage between the deep and shallow structural levels. Combining this with expansion indices (i.e. the ratio of the hanging wall to footwall thickness) allows us to place this geometric evolution into a temporal framework and to determine when the fault was active. For a specific horizon, throw and expansion indices are plotted at the midpoint between the hanging wall and footwall cut-offs (Baudon & Cartwright, 2008). In order to fully account for all deformation associated with the fault we measure both brittle (faulting of the host rock) and ductile (near-fault folding) components of deformation. To incorporate the ductile folding into our analysis we project horizons towards the fault from areas unaffected by local fault-parallel folding (Duffy et al., 2015; Long & Imber, 2012).

We choose not to depth convert or decompact our data when undertaking fault analyses so as not to introduce additional errors into our measurements. Related to this, we take the vertical component of displacement (fault throw measured in two-way-travel time) rather than displacement to avoid the need to depth convert the data. Due to the relatively layer-cake geometry of the stratigraphy across the Laminaria High, we do not expect any major lateral changes in lithology or velocity structure along the fault. One of the key tenets of our quantitative analysis is that the absolute throw values measured on the plots are less important than the overall shape of the throw profile, it is this latter information that provides key insights into how the faults evolved.

4 | RIFT PHYSIOGRAPHY

The Laminaria High is characterised by an E–W-trending fault population at deep structural levels, and a WSW–ENE-trending fault population at shallow levels (Figure 3). Here, we describe these fault populations in turn by examining rift physiography across Deep (H80), Intermediate (H75), and Shallow (H25) horizons (Figure 3), before analysing how the fault populations link across these structural levels.

4.1 | Basement horizon (H80) – Deep fault population

At deep structural levels, the Laminaria High is characterised by an E–W-striking fault population, herein termed the deep fault population, which we infer formed in response to Late Jurassic rifting across the NW shelf of Australia (Langhi & Borel, 2008). Faults within the deep fault population are commonly segmented, with individual segments ca. 5–10 km in length (Figure 3). The faults define a series of horst and graben, with a large horst present in the south of the area (Figure 3). They typically terminate upwards around the top Albian (H75) horizon (Figure 2a).

4.2 | Intermediate horizon (H75) and the MIU

We take the top Albian (H75) surface to represent the intermediate horizon between the deep and shallow fault populations, and a horizon within the MIU (Figure 2; Ciftci & Langhi, 2012). Few faults are present across this surface, with only the larger faults of the deep fault population, such as those defining the main horst structures, expressed. Although the majority of faults within the underlying deep fault population tip out beneath this horizon (Figure 2), local relief is generated due to differential compaction across the buried faults (Figure 3).

Above the intermediate horizon, we identify a prominent high-amplitude reflection within the MIU (Figure 2a). This horizon displays a negative impedance contrast with respect to overlying strata, is laterally discontinuous and is offset by numerous small-offset faults that seemingly do not extend far vertically within the section (Figure 2a). The laterally discontinuous nature of the horizon appears to correspond to areas where it is cross-cut by a series of channels. These channels trend roughly E–W across the area, are ca. 0.1 s TWT deep and 1–2 km wide, and are characterised by low-amplitude reflectivity (Figures 2a and 3b).

4.3 | Shallow horizon (H25) – Shallow fault population

At shallow depths, the Laminaria High is characterised by a WSW–ENE-trending fault population, with some E–W-striking structures also present, which we here term the shallow fault population. These faults formed in response to lithospheric flexure associated with subduction to the north (Saqab et al., 2017). Faults within the shallow fault population are typically segmented and often display en-echelon geometries (Figure 3). Towards shallower depths, the faults are also often associated with numerous antithetic and synthetic splays (Figure 2a). Faults within the shallow fault population extend upwards close to the seabed (Figure 2). They typically terminate downwards in the MIU, although individual structures link with the deep fault population (see Fault A on Figure 3).

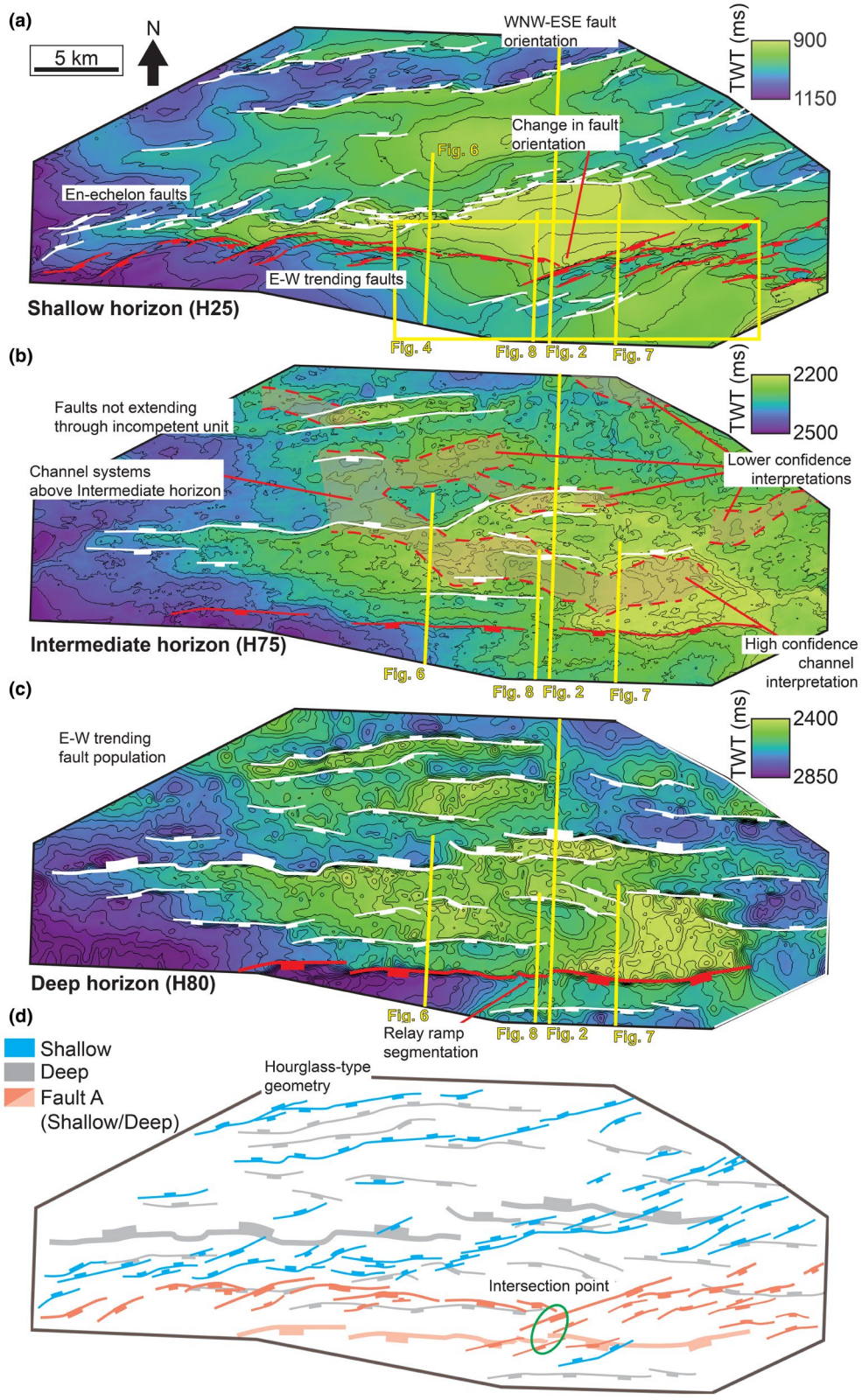

FIGURE 3 TWT structure maps of different horizons across the Laminaria High. (a) The shallow (H25) horizon. (b) Intermediate (H75) horizon. The majority of faults at this level do not extend through to the Shallow horizon. The channels are located above the horizon, see Figure 2. (c) E–W-trending faults expressed across the Deep horizon (H80). (d) Overlaid faults of the shallow and deep fault populations. Fault A is highlighted in red

4.4 | Connecting deep and shallow structural levels

Graben at shallow structural levels are often located above horst structures at deeper levels in plan-view, forming 'hourglass' geometries in cross-section (Figures 2 and 3; Çiftçi & Langhi, 2012). An exception to this is present in the south of the area, where a large horst is present at both the deep and shallow structural levels, defined by the same E–W-striking faults (Figure 3). We focus on a S-dipping fault along the southern margin of this horst, which is expressed at both the deep and shallow structural levels and is here termed Fault A (Figure 3). Within the deep fault population, Fault A forms a ca. 30 km long E–W-striking structure comprised of at least three ca. 10 km long segments separated by relay ramps. The western end of the fault extends out of the seismic survey at this depth, although the fault is observed to continue following an E–W orientation westwards across the Intermediate (H75) horizon (Figure 3).

In the west of the area Fault A is expressed within the shallow fault population as an E–W-trending structure. At shallow levels, the E–W orientation of Fault A differs from the prevailing WSW–ENE orientation of the shallow fault population (Figure 3). To the east, the shallow section of Fault A is aligned along a WSW–ENE orientation, with the west and east segments separated by a relay ramp (Figure 4). A similar, although less pronounced, change in orientation from E–W to ENE–WSW also occurs at the western end of Fault A at shallow depths, where the fault also displays a right-stepping en-echelon geometry (Figure 3). In the east, both the WSW–ENE-trending shallow segment and the E–W-trending deep segment of Fault A terminate in and are decoupled across the MIU.

Across the shallow horizon, the transition from an E–W-striking basement-linked fault segment in the west to a WSW–ENE-striking decoupled fault segment in the east forms a prominent intersection point, where the E–W section of Fault A in the west terminates in the footwall of WSW–ENE-striking section to the east (Figure 4). There is no lateral geometric linkage between the fault sections across the Shallow horizon, although this does not discount geometric linkage at deeper levels. The relay ramp formed between the two segments dips and widens towards the west (Figure 4). The ENE–WSW section of the fault is associated with a series of en-echelon antithetic faults in its hanging wall, forming a narrow graben. Three S-dipping en-echelon faults are also present in the hanging wall of Fault A, immediately outboard of the intersection (Figure 4). The intersection between the E–W and WSW–ENE fault segments across the Shallow horizon correlates with a relay ramp along Fault A across the Deep horizon, termed the 'Intersection point' (Figure 3).

5 | KINEMATICS AND VERTICAL COUPLING ALONG THE FAULT

We undertook *T-x* and *T-z* analyses along Fault A. Throw-length (*T-x*) analysis allowed us to constrain the distribution of throw at various structural levels (Figure 5), whereas throw-depth (*T-z*) analysis offers insights into how the fault evolved and the degree of coupling between deep and shallow sections of the fault (Figures 6 and 7).

Examining the *T-x* plots, throw along Fault A across the Deep horizon (H80) reaches a maxima of 323 ms in the centre of the fault (crossline #30, ca. 20 km; Figure 5). A further maxima of ca. 258 ms TWT is present towards the east (crossline #51; Figure 5). No data are available for the western end of the fault across the Deep horizon as the fault extends out of the volume. Multiple throw minima are identified at this depth, likely representing areas of relay ramp segmentation (Figure 3; e.g. Walsh et al., 2003). A prominent minima of 51 ms throw is present at ca. 30 km (crossline #46; Figure 5). Along the Intermediate horizon the throw profile displays two broad maxima of ca. 100 and ca. 112 ms TWT at ca. 20 km (crossline #30) and ca. 35 km (crossline #52), respectively, separated by a minima of 12 ms at ca. 30 km (crossline #45). Fault A extends out of the area on this horizon around crossline #11 (ca. 7–8 km).

Throw across the shallow horizon is typically higher than that of the intermediate horizon and less than that of the Deep horizon. Across this surface, extension is accommodated by multiple en-echelon fault segments (Figure 5). Individual throw deficits between

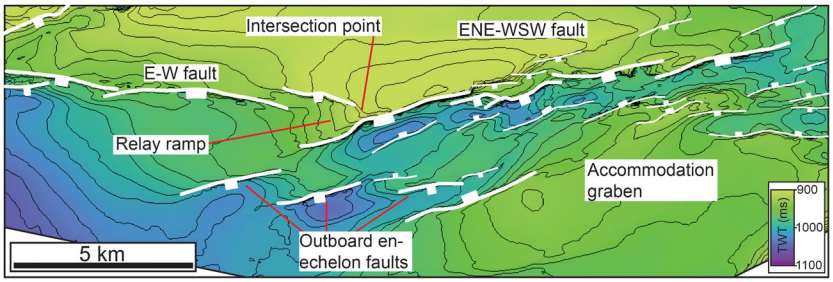

FIGURE 4 TWT structure map showing a closeup view of the intersection between the E–W and WSW–ENE segments of Fault A across the Shallow (H25) horizon. See Figure 3a for location

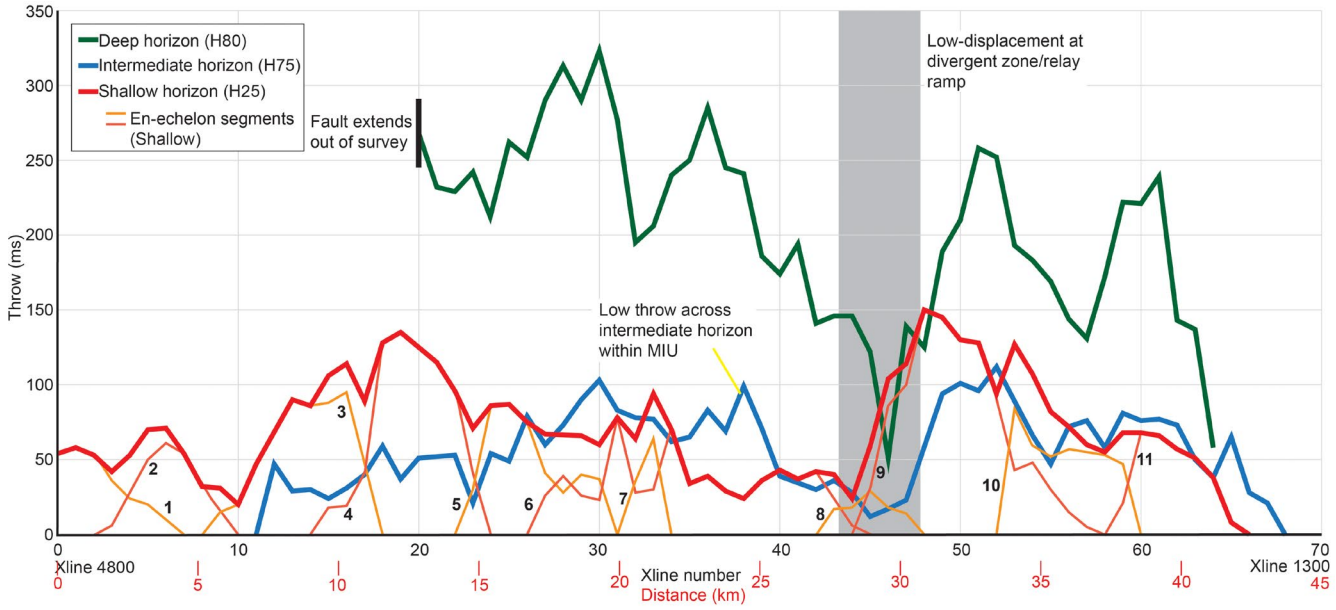

FIGURE 5 Throw-length plots along Fault A across the Deep, Intermediate and Shallow horizons. Throw measurements were calculated along the same crosslines to allow for comparison. The fault at the Deep horizon extends out of the seismic volume in the west. Individual segments of the fault at shallow depths are shown in orange and pink, with the cumulative throw shown in red

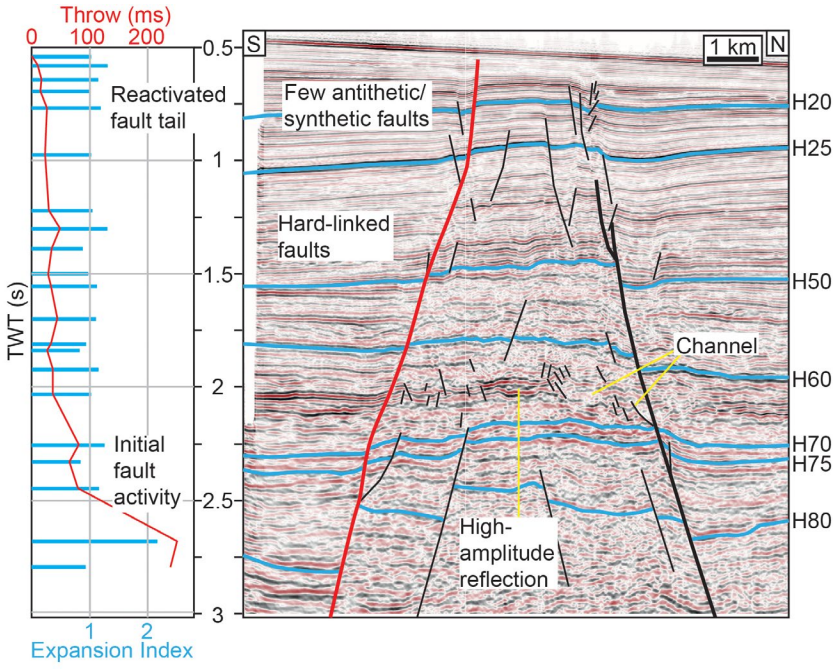

FIGURE 6 Interpreted seismic section and throw-depth plot of the hard-linked section of Fault A (red) in the west of the area. The thick black line represents the E–W-trending, N-dipping fault on the opposite side of the horst. See Figure 3 for location. Uninterpreted version of this section can be found in Figure S2

en-echelon segments are largely removed in the cumulative profile (Walsh et al., 2001). The cumulative throw profile across the Shallow horizon displays two distinct maxima of 135 ms 150 ms at ca. 12 km (crossline #19) and ca. 32 km (crossline #48) respectively, separated by a minima of 24 ms at ca. 28 km (crossline #44). The distribution of maxima and minima along the Shallow horizon is similar to that of the Intermediate horizon. A commonality between the displacement profiles is the presence of an area of low throw around 30 km along the length of the fault (around crossline #45). This corresponds to the 'Intersection point' along Fault A, represented by a relay ramp at the Deep horizon, and the intersection point on the shallow horizon (Figures 3 and 4). Across the Shallow horizon, this common minima separates the hard-linked E–W segment of Fault A in the west from the soft-linked decoupled section of the fault in the east.

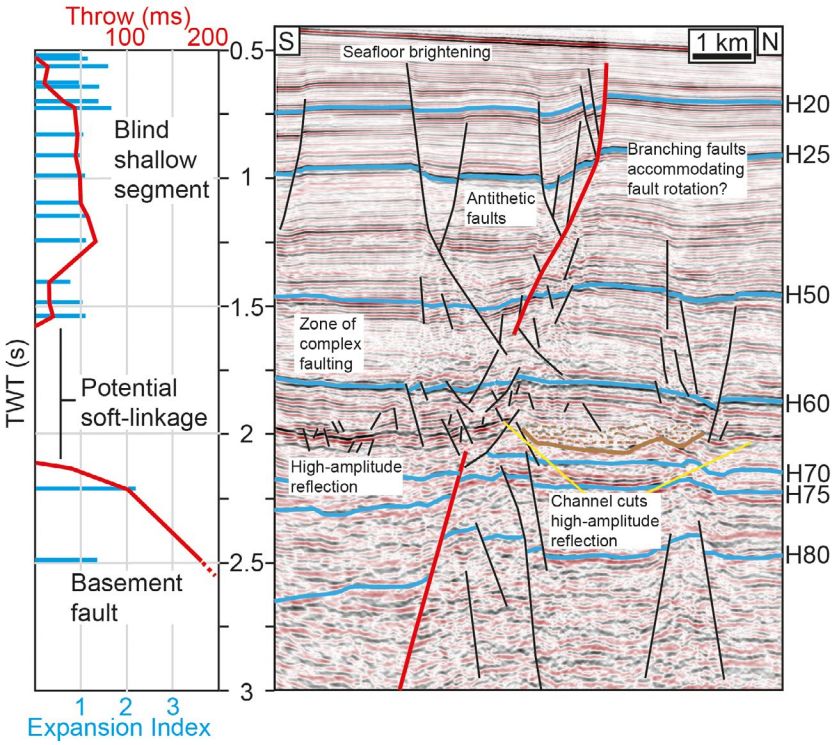

FIGURE 7 Interpreted seismic section and throw-depth plot of the soft-linked section of Fault A (red) in the east of the area. See Figure 3 for location. Uninterpreted version of this section can be found in Figure S3

5.1 | Hard-linked fault segment

In the west, Fault A forms an E–W-striking structure that extends throughout the section and links the deep and shallow fault populations. Similarly, a N-dipping fault on the northern margin of the horst also displays an E–W strike and extends through the MIU towards shallower depths, although this fault does not reach the Shallow Horizon as a single structure (Figures 3 and 6). Fault A displays an en-echelon geometry toward shallow depths with few associated antithetic faults. Throw-depth analyses show a maxima of ca. 250 ms within the Jurassic interval at ca. 2.5 s TWT, with a long tail of ca. 50 ms throw extending upwards for 2 s TWT to just beneath the present-day seabed (Figure 6). High-amplitudes across the seabed likely represent carbonate cementation following fluid flow along the faults, suggesting that, at the sub-seismic scale, these faults likely reach the seabed (Abdulkareem et al., 2019). Expansion indices display a maxima of ca. 2.1 at deeper levels (2.5–3 s TWT) and remain ca. 1 towards the upper fault termination. The throw maxima in the Jurassic interval indicates that the fault initiated in this interval. In addition, the thickening of the Jurassic interval into the hanging wall of the fault and the associated high expansion index indicates the fault was active at this time; we suggest this activity likely corresponds to the regional Late Jurassic rift phase (Figure 6). We interpret that the low-throw fault upper tail corresponds to a period of later activity as the fault was reactivated and propagated upwards through the succession. We relate this later reactivation to Pliocene-Pleistocene extension in response to regional subduction-related flexure (Figure 1b). Subtle hanging wall thickening and slightly elevated expansion indices at shallow levels may corroborate this interpretation although they are not conclusive.

5.2 | Soft-linked WSW–ENE fault segment

In contrast to the western section of the fault, there is no geometric linkage between the E–W-striking section of Fault A at deep structural levels and the WSW–ENE-striking shallow section of Fault A in the east (Figures 3 and 7). Here, the deep section of the fault terminates upwards within the MIU, whereas the shallow section terminates downwards at around 1.6 s TWT, above the H60 horizon and the MIU. The shallow fault section is associated with numerous antithetic fault segments. The area between the fault segments is characterised by a high-density of low-displacement, vertically restricted faults (Figure 7). We note that the High-amplitude reflection shows no significant offset related to either the deep or shallow sections of the fault, suggesting no geometric linkage between the two.

Throw-depth analyses highlight a throw maxima of ca. 200 ms at ca. 2.5 s TWT within the Jurassic interval, similar to the hard-linked segment of the fault to the west. The expansion index at this depth reaches ca. 2, again similar to the western segment. The *T-z* plot for the shallow section of the fault is characterised by a single throw maxima

in the centre (ca. 60 ms TWT at 1.25 s TWT), decreasing to zero at its upper and lower tips (ca. 0.5 and ca. 1.5 s TWT respectively). Expansion indices cluster around 1 throughout this interval although they increase to around ca. 1.5 above 0.75 s TWT, above the Base Pliocene (H20) horizon (Figure 7).

The Jurassic throw maxima and high expansion index at depth suggest late Jurassic activity along the fault, as identified along the hard-linked fault segment to the west (Figure 6). Similarly, based on the high expansion index above H20, we suggest that the shallow section of the fault formed in response to Pliocene–Pleistocene extension. However, in contrast to the western section of the fault, we suggest that this formed as a blind structure, initiating around the shallow throw maxima, rather than the upward propagation of the basement fault section (Figure 7). The zone of complex faulting between the shallow and deep sections of the fault in this area suggests soft linkage between the shallow and deep fault populations. Some strain is dissipated within the MIU and some accommodated by the smaller faults, which traverse the MIU.

5.3 | En-echelon faults

Three en-echelon faults are located in the hanging wall of Fault A, outboard of the intersection between the E–W and ENE–WSW oriented fault segments (Figure 4). These right-stepping, S-dipping faults are within the shallow fault population only and do not link to any faults in the deep fault population, instead terminating at depth above the MIU (Figure 8). The vertical linkage between the deep section of Fault A and the ENE–WSW and E–W shallow sections cannot be resolved in this area.

Kinematic analyses (T-z) of the central en-echelon fault shows a bell-shaped displacement profile with a throw maxima of ca. 65 ms from 1 to 1.25 s TWT, decreasing to zero at the upper (ca. 0.5 s TWT) and lower (1.75 s TWT) tips of the fault. Based on (1) the lack of distinct growth strata in the hanging wall of the fault; (2) the relatively constant expansion index of ca. 1 along the fault and (3) the bell-shaped displacement curve, we interpret that this fault formed as a blind structure in the hanging wall of Fault A (Figures 4 and 8).

6 | DISCUSSION

We have documented along-strike changes in the reactivation of a buried, pre-existing fault, and its coupling with younger faults at shallow depths. We find that this change in vertical coupling and reactivation influences the degree of structural inheritance that is present within the later-formed shallow fault population. The deep and shallow fault populations are largely decoupled across a mechanically weak, shale-dominated stratigraphic interval, the MIU. Here, we explore how both the geometry of the deeper fault and the character and thickness of the MIU influence hard- and soft-linkage between the Shallow and deep fault populations. We first discuss the geometry and character of the MIU and how it varies across the area, before discussing how the shallow and deep sections of Fault

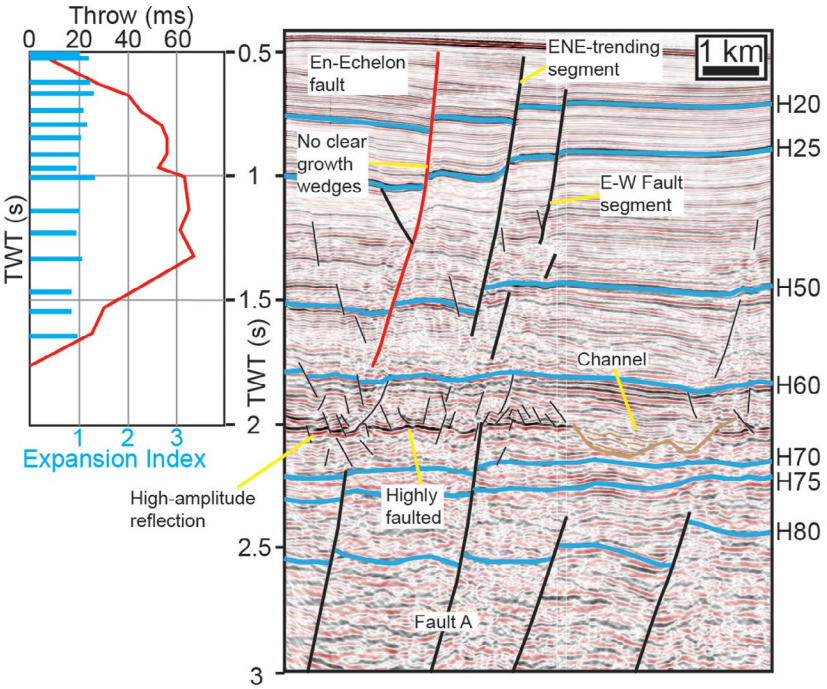

FIGURE 8 Interpreted seismic section and throw-depth plot of the central en-echelon fault segment (red), located in the hanging wall of Fault A. See Figure 3 for location. Uninterpreted version of this section can be found in Figure S4

A link across it and how changes in this linkage influence fault geometry at shallow depths.

6.1 | Geometry and composition of the MIU

The deep fault population is decoupled from the Shallow Fault Population across the Laminaria High by a mechanically incompetent, shale-dominated stratigraphic interval, which we here refer to as the MIU after Çiftçi and Langhi (2012; Figures 2 and 9). The geometry of this interval and the lateral and vertical distribution of strength within it may have a strong influence over the degree of coupling between the deep and shallow fault populations. Similar examples of mechanically weak intervals fully or partially decoupling vertically stratified fault populations are commonly identified in evaporite (e.g. Jackson & Lewis, 2016; Lewis et al., 2013; O'Sullivan et al., 2021) or shale-dominated intervals (Shipilin et al., 2020). The thickness and composition of the weak interval bears a strong influence on how faults link and how strain may be transferred across the interval. For example, the relative proportions of strong carbonate and weaker halite within evaporitic sequences influences the relative strength of the evaporitic sequence. We here explore the character of the MIU to investigate whether it may have influenced the observed changes in vertical coupling along Fault A.

The MIU spans Late Jurassic to Palaeocene strata and is 0.75–1 s TWT thick across the area (Figure 2). Faults of the deep fault population terminate upwards at the base of the MIU around the H75 horizon, whereas those in the shallow population terminate downwards into the top of the MIU around the Late Cretaceous–Early Cenozoic interval (H60; Figure 2). Based on uniaxial compressive strength as calculated from p-wave sonic logs, Çiftçi and Langhi (2012) define a ca. 500 m thick incompetent interval beginning at H80 and extending upwards to between H70 and H60, which they refer to as the MIU (Figure 2). The weakest interval within the MIU corresponds to a claystone interval situated below the H70 horizon and above the Valanginian Unconformity, between H75 and H80.

The composition and geometry of the MIU varies laterally and with depth across the Laminaria High. The interval that encompasses the MIU thins regionally towards the north and the east. We identify a prominent high-amplitude reflection between H70 and H60, seemingly located towards the top of the MIU (Figure 2). The reflection is characterised by a high amplitude and negative impedance contrast, is offset by numerous low-displacement faults that do not extend vertically into the section, and is laterally discontinuous over 2–3 km intervals (Figures 2 and 7). We note that the distribution of faulting is greater above the high-amplitude reflection than below (Figures 2, 7 and 8), with the fault density greatest at areas of interaction between the shallow and deep fault populations. In addition, the reflection is strata-concordant and often separates reflective strata above from more acoustically transparent strata below (Figure 8). The high-amplitude and negative polarity of the reflection indicate a relatively abrupt downwards decrease in acoustic impedance. Based on this, we suggest that the high-amplitude reflection represents an interface between relatively competent and strong carbonates above and a weaker shale-dominated interval below. This may represent a shelf-slope break unconformity at the Base Cenozoic and the top of the MIU (Figure 2b; Abbassi et al., 2015). Diagenetic processes occurring at this time may have led to the development of a hardground, producing the observed high-amplitude reflection. In addition, we suggest that the low-displacement faults offsetting the horizon represent a transition between deformation accommodated by large, localised faults in the stronger intervals above, diffuse faulting approaching the MIU, with ductile strain dominant within the MIU itself. The laterally discontinuous nature of the high-amplitude reflection appears to relate to later truncation by E–W-trending channel systems (Figures 2, 7 and 8). These channels are ca. 0.1 s TWT deep, 1–2 km wide and are characterised by low-amplitude reflectivity that onlap the channel margin (Figures 6 and 8). We speculate that these channel systems may correspond to the Eocene Grebe sandstone (Figure 2b; Abbassi et al., 2015), with the Laminaria High representing a relatively shallow marine environment at the time.

6.2 | Variable coupling between deep and shallow fault populations – The influence of the MIU and fault geometry

Although the MIU largely decouples the deep and shallow fault populations across the Laminaria High, the presence of 'hour-glass' structures, where shallow graben are co-located above deeper horsts, suggests some strain transference vertically between intervals (Figure 2). The style of linkage changes along Fault A, from coupled deep and shallow faults in the west, to decoupled structures in the east. A key question is whether this along-strike variation in coupling relates to the geometry and composition of the decoupling MIU, or the geometry and reactivation of the deeper, pre-existing portion of Fault A.

During the second extension phase, the reactivation and upwards propagation of deeper faults was inhibited by the MIU, which accommodated strain in a

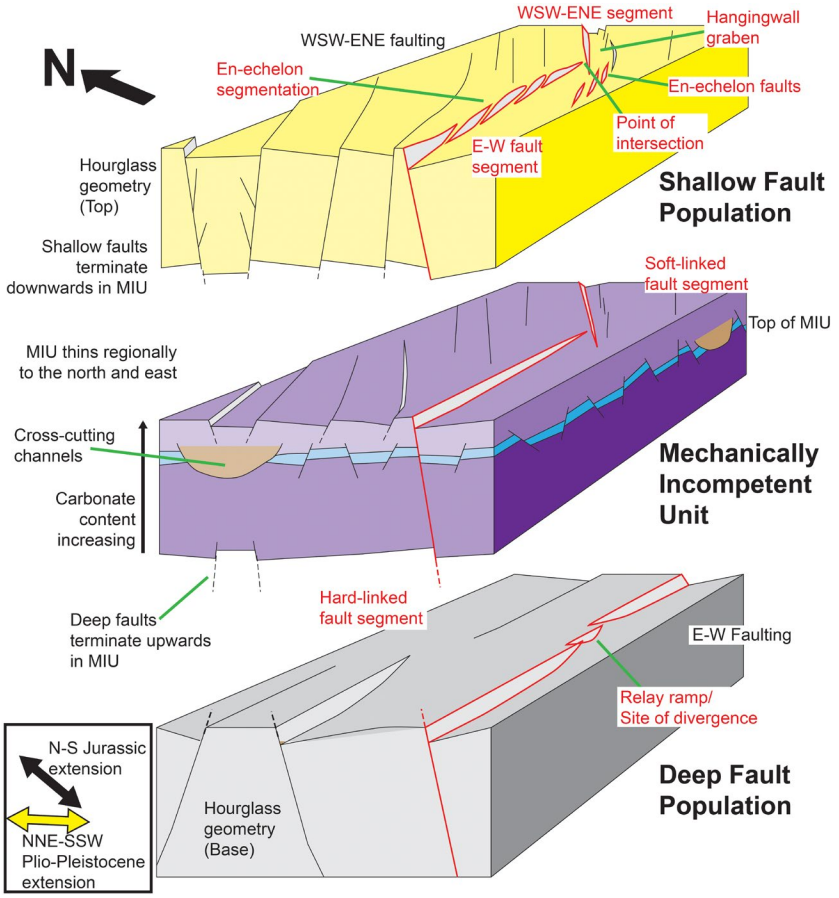

FIGURE 9 Schematic block model showing the different structural levels and fault populations across the Laminaria High, along with the relationships between them. Faults within the deep and shallow fault populations terminate at the base and top of the mechanically incompetent unit (MIU) respectively, with the exception of Fault A, shown in red

ductile manner (Figure 9). Rather than the reactivation of faults within the deep fault population, strain during Plio-Pleistocene extension was largely accommodated by faults that nucleate at shallow depths. Due to local stress variations related to the deeper fault population, faults within the shallow fault population typically form above the deeper horst structures, with the shallow faults then propagating downwards and terminating within the MIU, forming the hourglass shape (Çiftçi & Langhi, 2012). Furthermore, as Plio-Pleistocene extension was associated with regional subduction-related flexure to the north (Saqab et al., 2017), extensional stresses may be greater at shallow depths, leading to enhanced outer-arc extension related faulting at shallow structural levels, as opposed to the reactivation of deeper structures.

An exception to these hourglass geometries is Fault A, which forms an E–W-trending structure in the west that extends through the MIU and connects the deep and shallow fault populations (Figures 6 and 9). To the east, the shallow and deep segments of Fault A are decoupled across the MIU, with the shallow segment comprised of multiple en-echelon structures, that may link together above the MIU at depth and display an overall WSW–ENE orientation (Figure 7). This change in fault style suggests that the amount of strain transferred between deep and shallow structural levels vertically across the MIU changes along Fault A.

A key question therefore, is whether this along-strike change in vertical coupling along Fault A is driven by variable composition and properties of the MIU, or the geometry of Fault A within the deep fault population.

The thickness of the MIU changes regionally across the Laminaria high, thinning towards the north and east (Figure 9). A thicker incompetent interval may more efficiently partition strain and decouple fault populations. The thickness of ductile salt intervals has been shown to exert a strong control on strain transfer between sub- and supra-salt fault systems, with thicker ductile intervals promoting increased decoupling (Lewis et al., 2013). Similarly, albeit at a much larger scale, analogue modelling of crustal processes highlight how thick and weak lower crustal intervals effectively partition the strong upper mantle from the brittle upper crust (Zwaan et al., 2021). Changes in the composition of the decoupling interval also exert a strong effect on the degree of strain transfer that may occur across it; for example, more carbonate prone evaporite intervals may be relatively stronger than halite-dominated sequences (Lewis et al., 2013; O'Sullivan et al., 2021). In addition, higher strain rates may also promote coupling between vertically stratified intervals (Brun, 1999). However, although the thickness of the MIU changes

regionally across the area, this does not correlate with any systematic variation in coupling between shallow and deep fault populations (Figure 3). For example, the reactivated western segment of Fault A extends through the supposedly thicker section of the MIU in the west.

Minor changes in the thickness of the MIU may occur as a result of the underlying horst and graben structure of the deep fault population, with thinner intervals across the horsts and thicker intervals across the graben. This relief at the base of the MIU exerts a strong influence over the location of the hourglass structures within the shallow fault population (Çiftçi & Langhi, 2012). Here, we observe changes in coupling occurring along-strike of Fault A and parallel to the horst and graben structure, suggesting a different mechanism to that forming the hourglass structures. Furthermore, the shallowest section of the base MIU surface (H80, Figure 3a) occurs beneath the eastern segment of Fault A, where shallow and deep sections of the fault are decoupled. Lateral lithological changes within the MIU, such as truncation by channels, effectively reduce the thickness of the MIU and may cause abrupt changes in its overall competency. Although cross-cut by channels across parts of the Laminaria High, we identify no channel features within the MIU crossing Fault A, and in particular we do not identify any channels that correspond to the intersection point (Figure 3b). These observations suggest that lateral changes in the competency of the MIU, either related to its thickness or composition do not account for the abrupt along-strike transition from soft- to hard-linkage observed along Fault A.

Having shown that the geometry and properties of the MIU do not appear to influence the degree of coupling along Fault A, we now examine the potential influence of the deep fault geometry. In the deep fault population, Fault A displays two throw maxima, separated by a prominent minimum at ca. 30 km distance along the fault that persists in the same location across all structural levels (Figure 5). Across the Deep horizon, it corresponds to a relay ramp along the fault, whereas at shallow depths, it corresponds to the intersection points between the E–W and WSW–ENE-trending fault segments (Figure 4). The relay ramp across the Deep horizon may contain an internal small fault segment, although this is difficult to resolve, or may be between two underlapping segments (Figure 3). A further relay ramp is present along the fault to the west although this appears to have little influence over fault geometry and reactivation, with a less developed throw minima (Figures 3c and 5).

Fault A is one of the largest faults across the Laminaria High, forming the southern boundary to a major horst. Throw across the Deep horizon is greatest to the west of the relay ramp at the intersection point, that is, the segment that was reactivated (Figures 3 and 5). Observations regarding the evolution of normal fault systems and potential inversion suggest that larger structures are more likely to localise strain and reactivate than smaller ones (Reilly et al., 2017; Walsh et al., 2001). Accordingly, we suggest that Fault A, and in particular its western segment, may represent one of those most likely to reactivate. Similarly, the northern boundary fault to this horst also appears to reactivate and propagate through the MIU (Figure 6).

We suggest that the high-displacement, western segment of Fault A reactivated during Plio-Pleistocene extension and was able to propagate upwards through the MIU, forming an anomalously oriented structure within the developing shallow fault population (Figures 3, 6 and 9). The geometric complexity of a structure may also impact its likelihood to reactivate (Phillips et al., 2020). We suggest that the relay ramp along Fault A acted as a buffer to the reactivation and upwards propagation of the deep section of Fault A further east, where upwards propagation was inhibited by the MIU (Figure 9). Langhi and Borel (2008) identify a series of transverse accommodation zones located between E–W fault segments that they relate to the initial propagation and segmentation of the deep fault population. We speculate that such structures and the associated relay ramps may represent a manifestation of a deeper basement fabric, potentially related to earlier rift events, which would control both the initial location of the accommodation zone and therefore the subsequent relay. However, we are unable to confirm the presence of such as fabric within the data. Similar examples of faults being segmented by pre-existing structures and fabrics have been documented in the North Sea (Duffy et al., 2015; Henza et al., 2011). Such a mechanism would potentially explain why the change in structural styles occurs in these locations and not at other relay ramps, although we are unable to confirm this.

Soft-linkage between shallow and deep sections of Fault A occurs east of the relay ramp. The shallow segment of Fault A strikes WSW–ENE, with a series of en-echelon antithetic faults forming a hanging wall graben to the south (Figures 4 and 7). We suggest that this antithetic graben forms to accommodate strains associated with the divergence between the WSW–ENE oriented shallow fault segment and the E–W deep fault segment to the east. As the shallow and deep fault segments diverge eastwards, the degree of linkage between them diminishes. A similar situation occurs where faults form in close proximity to pre-existing structures. Collanega et al. (2019) show how faults may initially form independently in the shallow cover, oriented perpendicular to the regional stress field and then rotate into a local stress field associated with the underlying structure as they propagate downwards. Faults directly associated with pre-existing structures, as is the case here, may initially align with the pre-existing

structure, and then rotate to align with the regional stress field as they propagate upwards. A further example of this occurs at the western end of Fault A, where the shallow fault begins to rotate to a more WSW–ENE orientation. Here, we suggest that the deep section of the fault is no longer present, having terminated further east, allowing the shallow section to rotate into the regional stress field.

6.3 | Accommodating strain across the intersection point between misaligned E–W and WSW–ENE oriented faults

The shallow section of Fault A in the west is anomalously oriented with respect to others in the shallow fault population, being hard-linked to the fault within the deep fault population (Figures 3 and 9). The majority of faults within the shallow fault population, including the eastern shallow segment of Fault A, are oriented WSW–ENE, paralleling the subduction zone to the north (Figure 1). During the latter phase of extension, faults within the deep fault population are non-optimally oriented with respect to the prevailing NNE–SSW stress field. These pre-existing faults, such as the western segment of Fault A, may locally reorient the regional stress field, such that they experience dip-slip activity while being oblique to the regional stress field, and also to those faults that formed decoupled and independent from deeper structures. Similar observations of reactivated pre-existing structures locally perturbing the regional stress field have been made in the East African Rift (Philippon et al., 2015) and onshore Norway (Fossen et al., 2017), as well as in analogue modelling (e.g. Samsu et al., 2021).

Alternatively, when a pre-existing fault is oriented oblique to the regional stress field, strain may be partitioned into strike-slip and dip-slip components such that the fault experiences oblique slip (Giba et al., 2012; Phillips et al., 2018). We note that the western segment of Fault A is highly segmented, with individual segments displaying an en-echelon geometry (Figure 3). En-echelon fault geometries may form through the oblique reactivation of a pre-existing fault (Giba et al., 2012; Grant & Kattenhorn, 2004; Withjack et al., 2017), or dip-slip activity within a mechanically anisotropic unit (Jackson & Rotevatn, 2013; Schöpfer et al., 2007). Aside from the broad changes in mechanical strength through the section illustrated by the MIU, we do not see such anisotropy within the stratigraphy at shallow depths. In addition, the WSW–ENE-trending faults in the north of the area display a much more linear geometry (Figure 3). Accordingly, we suggest that the en-echelon geometry of the western segment of Fault A indicates oblique reactivation of the deeper fault. Although the fault displays an overall E–W orientation, each individual segment displays a more optimal geometry as it rotates toward the regional stress field at its tips. Similarly, where the overall orientation of the Shallow section of Fault A changes from E–W to WSW–ENE to the west, we suggest that this may relate to the fault no longer being present within the deep population, or having a limited effect, as in the eastern segment. As the influence of the deep section of Fault A diminishes to the west, the shallow faults become more influenced by the regional NNW–SSE stress field at the time.

As well as a transition from hard- to soft-linkage, the intersection point also represents a transition from oblique activity in the west to dip-slip activity in the east, at least at shallow depths. This area is associated with three en-echelon faults outboard of the intersection and a high density of faulting immediately above the MIU (Figure 8). The intersection between the E–W and WSW–ENE fault segments represents a transition from optimally to non-optimally oriented fault segments and an associated transition from oblique to dip-slip activity from west to east (Figure 9). Local stress interactions associated with these transitions may lead to additional faulting and fracturing, and in this instance we suggest the development of the outboard en-echelon faults, to better accommodate the regional stress field in this area (Gartrell et al., 2004). We suggest that these faults may serve a similar function to release faults identified in the hanging wall of larger structures, which accommodate stresses relating to other structures within a local stress field (Destro, 1995). Similar examples where hanging wall faults accommodate stresses associated with changes in fault orientation have also been documented in the North Sea (Phillips et al., 2018).

7 | CONCLUSIONS

In this study we document the geometric and kinematic evolution of a reactivated, buried fault in the Laminaria High, highlighting how vertical coupling between structural levels changes along-strike. We show how in the presence of a decoupling interval, and the reactivation and geometry of a deeper structure may influence the degree of geometric and kinematic linkage to shallower, newly forming faults. In particular, we find that:

- The Laminaria High is characterised by an E–W-trending fault population at depth formed during Late Jurassic rifting, and a WSW–ENE fault population at shallow depths formed due to flexure associated with the Timor Subduction zone to the north. The majority of faults within these populations are vertically separated and decoupled across a MIU comprised predominately of shales.

- Some faults in the area extend through the mechanically incompetent interval, of which we focus on one fault in particular, Fault A. At shallow depths, the western segment of the fault is oriented E–W following the orientation of the deep fault population, whereas the eastern segment is not geometrically linked, and displays a WSW–ENE orientation consistent with other faults in the shallow fault population.
- As the western segment of Fault A, which follows the E–W orientation of the reactivated deeper structure extends upwards to shallow depths it begins to splay into a series of en-echelon segments, whereas individual segments rotate to the prevalent stress field within the shallow fault population. This produces an E–W arrangement of WSW–ENE en-echelon fault segments.
- This along-strike change in the degree of vertical coupling corresponds to an area of low-displacement and a relay ramp along the fault. We suggest that the reactivation and upwards propagation of Fault A in the west is inhibited further east at a relay ramp along the fault. Past the relay ramp, the shallow and deep segments display no geometric linkage although some strain transfer and soft-linkage is present. The eastwards divergence of the shallow and deep segments is accommodated by a series of antithetic faults.
- During NNW–SSE oriented Plio-Pleistocene extension, local stresses arising from the transition between the non-optimally oriented E–W fault segment in the west, to the more optimal WSW–ENE segment in the east are accommodated by a series of en-echelon structures formed outboard of the intersection between the two segments of Fault A at shallow structural levels.

ACKNOWLEDGEMENTS

The seismic data used in this study are publicly available from the Geoscience Australia Petroleum Data Repository (http://www.ga.gov.au/nopims). This work forms an output from a Leverhulme Trust Early Career Fellowship held by Phillips at the University of Durham. The authors would also like to thank Conor O'Sullivan and Anindita Samsu for two expert reviews that greatly improved the manuscript, as well as Zoe Mildon for editorial handling.

PEER REVIEW

The peer review history for this article is available at https://publons.com/publon/10.1111/bre.12626.

DATA AVAILABILITY STATEMENT

The data that support the findings of this study are openly available in the Geoscience Australia Petroleum Data Repository at (http://www.ga.gov.au/nopims).

ORCID

Thomas B. Phillips https://orcid.org/0000-0002-6783-9092

REFERENCES

Abbassi, S., di Primio, R., Horsfield, B., Edwards, D. S., Volk, H., Anka, Z., & George, S. C. (2015). On the filling and leakage of petroleum from traps in the Laminaria High region of the northern Bonaparte Basin, Australia. *Marine and Petroleum Geology*, *59*, 91–113. https://doi.org/10.1016/j.marpetgeo.2014.07.030

Abdulkareem, L., Imber, J., & Hobbs, R. (2019). Geophysical evidence for structurally-controlled, authigenic carbonate cementation in the Laminaria High, Bonaparte basin, Northwest Shelf of Australia. *Marine and Petroleum Geology*, *99*, 563–576. https://doi.org/10.1016/j.marpetgeo.2018.10.018

Baudon, C., & Cartwright, J. (2008). The kinematics of reactivation of normal faults using high resolution throw mapping. *Journal of Structural Geology*, *30*(8), 1072–1084. https://doi.org/10.1016/j.jsg.2008.04.008

Bell, J. (1996). *Petro geoscience 2. In situ stresses in sedimentary rocks (part 2): Applications of stress measurements*. Geoscience Canada.

Brun, J. P. (1999). Narrow rifts versus wide rifts: Inferences for the mechanics of rifting from laboratory experiments. *Philosophical Transactions of the Royal Society of London. Series A: Mathematical, Physical and Engineering Sciences*, *357*(1753), 695–712. https://doi.org/10.1098/rsta.1999.0349

Çiftçi, N. B., & Langhi, L. (2012). Evolution of the hourglass structures in the Laminaria High, Timor Sea: Implications for hydrocarbon traps. *Journal of Structural Geology*, *36*, 55–70. https://doi.org/10.1016/j.jsg.2011.12.006

Claringbould, J. S., Bell, R. E., Jackson, C. A. L., Gawthorpe, R. L., & Odinsen, T. (2017). Pre-existing normal faults have limited control on the rift geometry of the northern North Sea. *Earth and Planetary Science Letters*, *475*, 190–206. https://doi.org/10.1016/j.epsl.2017.07.014

Coleman, A. J., Jackson, C. A. L., & Duffy, O. B. (2017). Balancing sub-and supra-salt strain in salt-influenced rifts: Implications for extension estimates. *Journal of Structural Geology*, *102*, 208–225. https://doi.org/10.1016/j.jsg.2017.08.006

Collanega, L., Siuda, K., A.-L. Jackson, C., Bell, R. E., Coleman, A. J., Lenhart, A., Magee, C., & Breda, A. (2019). Normal fault growth influenced by basement fabrics: The importance of preferential nucleation from pre-existing structures. *Basin Research*, *31*(4), 659–687. https://doi.org/10.1111/bre.12327

de Ruig, M., Trupp, M. J., Bishop, D. J., Kuek, D., & Castillo, D. A. (2000). Fault architecture and the mechanics of fault reactivation in the Nancar Trough/Laminaria area of the Timor Sea, Northern Australia. *The APPEA Journal*, *40*, 174–193. https://doi.org/10.1071/AJ99010

Deng, C., Fossen, H., Gawthorpe, R. L., Rotevatn, A., Jackson, C. A., & FazliKhani, H. (2017). Influence of fault reactivation during multiphase rifting: The Oseberg area, northern North Sea rift. *Marine and Petroleum Geology*, *86*, 1252–1272. https://doi.org/10.1016/j.marpetgeo.2017.07.025

Destro, N. (1995). Release fault: A variety of cross fault in linked extensional fault systems, in the Sergipe-Alagoas Basin, NE Brazil. *Journal of Structural Geology*, *17*(5), 615–629. https://doi.org/10.1016/0191-8141(94)00088-H

Duffy, O. B., Bell, R. E., Jackson, C. A. L., Gawthorpe, R. L., & Whipp, P. S. (2015). Fault growth and interactions in a multiphase rift fault network: Horda Platform, Norwegian North Sea. *Journal of Structural Geology*, *80*, 99–119. https://doi.org/10.1016/j.jsg.2015.08.015

Fossen, H., Khani, H. F., Faleide, J. I., Ksienzyk, A. K., & Dunlap, W. J. (2017). Post-Caledonian extension in the West Norway–northern North Sea region: The role of structural inheritance. *Geological Society, London, Special Publications*, *439*(1), 465–486. https://doi.org/10.1144/SP439.6

Gartrell, A., Zhang, Y., Lisk, M., & Dewhurst, D. (2003). Enhanced hydrocarbon leakage at fault intersections: An example from the Timor Sea, Northwest Shelf, Australia. *Journal of Geochemical Exploration*, *78*, 361–365. https://doi.org/10.1016/S0375-6742(03)00125-0

Gartrell, A., Zhang, Y., Lisk, M., & Dewhurst, D. (2004). Fault intersections as critical hydrocarbon leakage zones: Integrated field study and numerical modelling of an example from the Timor Sea, Australia . *Marine and Petroleum Geology*, *21*(9), 1165–1179. https://doi.org/10.1016/j.marpetgeo.2004.08.001

Giba, M., Walsh, J. J., & Nicol, A. (2012). Segmentation and growth of an obliquely reactivated normal fault. *Journal of Structural Geology*, *39*, 253–267. https://doi.org/10.1016/j.jsg.2012.01.004

Grant, J. V., & Kattenhorn, S. A. (2004). Evolution of vertical faults at an extensional plate boundary, southwest Iceland. *Journal of Structural Geology*, *26*(3), 537–557. https://doi.org/10.1016/j.jsg.2003.07.003

Harrowfield, M., & Keep, M. (2005). Tectonic modification of the Australian North-West Shelf: Episodic rejuvenation of long-lived basin divisions. *Basin Research*, *17*(2), 225–239. https://doi.org/10.1111/j.1365-2117.2005.00251.x

Henstra, G. A., Kristensen, T. B., Rotevatn, A., & Gawthorpe, R. L. (2019). How do pre-existing normal faults influence rift geometry? A comparison of adjacent basins with contrasting underlying structure on the Lofoten Margin, Norway. *Basin Research*, *31*(6), 1083–1097. https://doi.org/10.1111/bre.12358

Henza, A. A., Withjack, M. O., & Schlische, R. W. (2010). Normal-fault development during two phases of non-coaxial extension: An experimental study. *Journal of Structural Geology*, *32*(11), 1656–1667. https://doi.org/10.1016/j.jsg.2009.07.007

Henza, A. A., Withjack, M. O., & Schlische, R. W. (2011). How do the properties of a pre-existing normal-fault population influence fault development during a subsequent phase of extension? *Journal of Structural Geology*, *33*(9), 1312–1324. https://doi.org/10.1016/j.jsg.2011.06.010

Jablonski, D., & Saitta, A. J. (2004). Permian to Lower Cretaceous plate tectonics and its impact on the tectono-stratigraphic development of the Western Australian margin. *The APPEA Journal*, *44*(1), 287–328. https://doi.org/10.1071/AJ03011

Jackson, C. A. L., & Lewis, M. M. (2016). Structural style and evolution of a salt-influenced rift basin margin; the impact of variations in salt composition and the role of polyphase extension. *Basin Research*, *28*(1), 81–102. https://doi.org/10.1111/bre.12099

Jackson, C. A. L., & Rotevatn, A. (2013). 3D seismic analysis of the structure and evolution of a salt-influenced normal fault zone: A test of competing fault growth models. *Journal of Structural Geology*, *54*, 215–234. https://doi.org/10.1016/j.jsg.2013.06.012

Keep, M., Clough, M., & Langhi, L. (2002). Neogene tectonic and structural evolution of the Timor Sea region, NW Australia. In M. Keep & S. J. Moss (Eds.), *The sedimentary basins of Western Australia 3*, Proceedings of the Petroleum Exploration Society of Australia Symposium, Perth (pp. 341–353).

Labutis, V. R., Ruddock, A. D., & alcraft, A. C. (1998). Stratigraphy of the southern Sahul Platform. *The APPEA Journal*, *38*(1), 115–136. https://doi.org/10.1071/AJ97006

Langhi, L., & Borel, G. D. (2005). Influence of the Neotethys rifting on the development of the Dampier Sub-basin (North West Shelf of Australia), highlighted by subsidence modelling. *Tectonophysics*, *397*(1–2), 93–111. https://doi.org/10.1016/j.tecto.2004.10.005

Langhi, L., & Borel, G. D. (2008). Reverse structures in accommodation zone and early compartmentalization of extensional system, Laminaria High (NW shelf, Australia). *Marine and Petroleum Geology*, *25*(8), 791–803. https://doi.org/10.1016/j.marpetgeo.2008.04.007

Langhi, L., Ciftci, N. B., & Borel, G. D. (2011). Impact of lithospheric flexure on the evolution of shallow faults in the Timor foreland system. *Marine Geology*, *284*(1–4), 40–54. https://doi.org/10.1016/j.margeo.2011.03.007

Langhi, L., Zhang, Y., Gartrell, A., Brincat, M. P., Lisk, M., Underschultz, J., & Dewhurst, D. (2013). 2. Mechanism of upfault seepage and seismic expression of hydrocarbon discharge sites from the Timor Sea. Hydrocarbon Seepage: From Source to Surface. *Society of Exploration Geophysicists and American Association of Petroleum Geologists*, *11*, 41. https://doi.org/10.1190/1.9781560803119.ch2

Lewis, M. M., Jackson, C. A. L., & Gawthorpe, R. L. (2013). Salt-influenced normal fault growth and forced folding: The Stavanger Fault System, North Sea. *Journal of Structural Geology*, *54*, 156–173. https://doi.org/10.1016/j.jsg.2013.07.015

Long, J. J., & Imber, J. (2012). Strain compatibility and fault linkage in relay zones on normal faults. *Journal of Structural Geology*, *36*, 16–26. https://doi.org/10.1016/j.jsg.2011.12.013

Nixon, C. W., Sanderson, D. J., Dee, S. J., Bull, J. M., Humphreys, R. J., & Swanson, M. H. (2014). Fault interactions and reactivation within a normal-fault network at Milne Point, Alaska. *AAPG Bulletin*, *98*(10), 2081–2107. https://doi.org/10.1306/04301413177

O'Sullivan, C. M., Childs, C. J., Saqab, M. M., Walsh, J. J., & Shannon, P. M. (2021). The influence of multiple salt layers on rift-basin development; the Slyne and Erris basins, offshore NW Ireland. *Basin Research*, *33*(3), 2018–2048. https://doi.org/10.1111/bre.12546

O'Brien, G. W., Etheridge, M. A., Willcox, J. B., Morse, M., Symonds, P., Norman, C., & Needham, D. J. (1993). The structural architecture of the Timor Sea, north-western Australia: Implications for basin development and hydrocarbon exploration. *The APPEA Journal*, *33*(1), 258–279. https://doi.org/10.1071/AJ92019

Philippon, M., Willingshofer, E., Sokoutis, D., Corti, G., Sani, F., Bonini, M., & Cloetingh, S. (2015). Slip re-orientation in oblique rifts. *Geology*, *43*(2), 147–150. https://doi.org/10.1130/G36208.1

Phillips, T. B., Jackson, C. A. L., Bell, R. E., & Duffy, O. B. (2018). Oblique reactivation of lithosphere-scale lineaments controls rift physiography–the upper-crustal expression of the Sorgenfrei-Tornquist Zone, offshore southern Norway. *Solid Earth*, *9*(2), 403–429. https://doi.org/10.5194/se-9-403-2018

Phillips, T. B., Jackson, C. A. L., & Norcliffe, J. R. (2020). Pre-inversion normal fault geometry controls inversion style and magnitude, Farsund Basin, offshore southern Norway. *Solid Earth*, *11*(4), 1489–1510. https://doi.org/10.5194/se-11-1489-2020

Reeve, M. T., Bell, R. E., Duffy, O. B., Jackson, C. A. L., & Sansom, E. (2015). The growth of non-colinear normal fault systems; What can we learn from 3D seismic reflection data? *Journal of Structural Geology*, *70*, 141–155. https://doi.org/10.1016/j.jsg.2014.11.007

Reilly, C., Nicol, A., & Walsh, J. (2017). Importance of pre-existing fault size for the evolution of an inverted fault system. *Geological Society, London, Special Publications*, *439*(1), 447–463. https://doi.org/10.1144/SP439.2

Samsu, A., Cruden, A. R., Molnar, N. E., & Weinberg, R. F. (2021). Inheritance of penetrative basement anisotropies by extension-oblique faults: Insights from analogue experiments. *Tectonics*, *40*(5). https://doi.org/10.1029/2020TC006596

Saqab, M. M., Bourget, J., Trotter, J., & Keep, M. (2017). New constraints on the timing of flexural deformation along the northern Australian margin: Implications for arc-continent collision and the development of the Timor Trough. *Tectonophysics*, *696*, 14–36. https://doi.org/10.1016/j.tecto.2016.12.020

Schöpfer, M. P., Childs, C., & Walsh, J. J. (2007). Two-dimensional distinct element modeling of the structure and growth of normal faults in multilayer sequences: 2. Impact of confining pressure and strength contrast on fault zone geometry and growth. *Journal of Geophysical Research: Solid Earth*, *112*(B10). https://doi.org/10.1029/2006JB004903

Shipilin, V., Tanner, D. C., von Hartmann, H., & Moeck, I. (2020). Multiphase, decoupled faulting in the southern German Molasse Basin–evidence from 3-D seismic data. *Solid Earth*, *11*(6), 2097–2117. https://doi.org/10.5194/se-11-2097-2020

Walsh, J. J., Bailey, W. R., Childs, C., Nicol, A., & Bonson, C. G. (2003). Formation of segmented normal faults: A 3-D perspective. *Journal of Structural Geology*, *25*(8), 1251–1262. https://doi.org/10.1016/S0191-8141(02)00161-X

Walsh, J. J., Childs, C., Meyer, V., Manzocchi, T., Imber, J., Nicol, A., Tuckwell, G., Bailey, W. R., Bonson, C. G., Watterson, J., Nell, P. A., & Strand, J. (2001). Geometric controls on the evolution of normal fault systems. *Geological Society, London, Special Publications*, *186*(1), 157–170. https://doi.org/10.1144/GSL.SP.2001.186.01.10

Whipp, P. S., Jackson, C. L., Gawthorpe, R. L., Dreyer, T., & Quinn, D. (2014). Normal fault array evolution above a reactivated rift fabric; a subsurface example from the northern Horda Platform, Norwegian North Sea. *Basin Research*, *26*(4), 523–549. https://doi.org/10.1111/bre.12050

Withjack, M. O., Henza, A. A., & Schlische, R. W. (2017). Three-dimensional fault geometries and interactions within experimental models of multiphase extension. *AAPG Bulletin*, *101*(11), 1767–1789. https://doi.org/10.1306/02071716090

Yeates, A. N., Bradshaw, M. T., Dickins, J. M., Brakel, J. M., Exon, N. F., Langford, R. P., Mulholland, S. M., Totterdell, J. M., & Yeung, M. (1987). The Westralian Superbasin: An Australian link with Tethys. In K. G. McKenzie (Ed.), *Shallow Tethys 2, International Symposium, Wagga Wagga, Balkema* (pp. 199–213). Rotterdam.

Zwaan, F., Chenin, P., Erratt, D., Manatschal, G., & Schreurs, G. (2021). Complex rift patterns, a result of interacting crustal and mantle weaknesses, or multiphase rifting? Insights from analogue models. *Solid Earth Discussions*, 1–38. https://doi.org/10.5194/se-2020-214

SUPPORTING INFORMATION

Additional supporting information may be found in the online version of the article at the publisher's website.

How to cite this article: Phillips, T. B., McCaffrey, K., & Magarinos, L. (2021). Influence of variable decoupling between vertically separated fault populations on structural inheritance – The Laminaria High, NW Shelf of Australia. *Basin Research*, 00, 1–17. https://doi.org/10.1111/bre.12626